

## Laser-ablated ZnO for thin films of ZnO and Mg x Zn ( 1 x ) O

R. K. Thareja, H. Saxena, and V. Narayanan

Citation: [Journal of Applied Physics](#) **98**, 034908 (2005); doi: 10.1063/1.1997287

View online: <http://dx.doi.org/10.1063/1.1997287>

View Table of Contents: <http://scitation.aip.org/content/aip/journal/jap/98/3?ver=pdfcov>

Published by the [AIP Publishing](#)

---

### Articles you may be interested in

[Effect of Mg content on structural, electrical, and optical properties of Li-doped Zn 1 x Mg x O thin films](#)  
Appl. Phys. Lett. **90**, 182116 (2007); 10.1063/1.2735555

[Synchrotron x-ray study of polycrystalline wurtzite Zn 1 x Mg x O \( 0 x 0.15 \) : Evolution of crystal structure and polarization](#)  
Appl. Phys. Lett. **90**, 101904 (2007); 10.1063/1.2711289

[Induced emission cross sections of near-stoichiometric Li Nb O 3 : Mg , Nd](#)  
J. Appl. Phys. **100**, 103501 (2006); 10.1063/1.2386913

[Sputtered Zn 1 x Ga 2 O 4 : Mn thin-film electroluminescent devices prepared using cadmium-assisted processing](#)  
J. Appl. Phys. **97**, 094502 (2005); 10.1063/1.1886889

[Structural and transport properties of Cu Sc 1 x Mg x O 2 + y delafossites](#)  
J. Appl. Phys. **96**, 6188 (2004); 10.1063/1.1806256

---



## Re-register for Table of Content Alerts

Create a profile.



Sign up today!



# Laser-ablated ZnO for thin films of ZnO and $\text{Mg}_x\text{Zn}_{(1-x)}\text{O}$

R. K. Thareja,<sup>a)</sup> H. Saxena, and V. Narayanan

*Department of Physics and Center for Laser Technology, Indian Institute of Technology Kanpur, Kanpur-208 016 (UP), India*

(Received 17 February 2005; accepted 21 June 2005; published online 5 August 2005)

We report investigations of ZnO plasma at various ambient pressures of oxygen produced by third harmonic 355 nm of neodymium: yttrium aluminum garnet laser for depositing quality nanocrystalline ZnO thin films. Time- and space-resolved optical emission spectroscopy is used to correlate the plasma properties with that of the deposited thin films. The temporally resolved images of the plumes are correlated with the time-resolved emission spectrum of plasma species in the plume. The deposited films of ZnO at 100 mTorr of ambient oxygen exhibited third-harmonic generation.  $\text{Mg}_x\text{Zn}_{(1-x)}\text{O}$  alloy thin films of different molar percentage of MgO were deposited on glass substrates with the aim of achieving variable band gap using pulsed laser deposition in 100-mTorr oxygen ambient at substrate temperatures ranging from 200 to 500 °C. The films with  $x=0.1$  and 0.3 exhibit single hexagonal phase with (002) as the preferred orientation, however, with  $x=0.5$ , a transition to mixed phase with hexagonal phase of (100) and cubic phase of (200) orientation is observed. The absorption edge is blueshifted with an increase of  $x$  and deposition temperature. The band gap of the deposited films increases with molar percentage and deposition temperature. The deposited films exhibited high degree of transparency (>85%) over visible range. © 2005 American Institute of Physics. [DOI: 10.1063/1.1997287]

## I. INTRODUCTION

Laser ablation is being widely used in various applications of material processing, such as thin-film deposition, cluster formation, chemical reactions, and surface modifications (synthesis of nanoclusters).<sup>1</sup> In particular, thin-film deposition called pulsed laser deposition (PLD) has emerged as one of the versatile techniques for the deposition of thin films of a variety of materials such as metals, semiconductors, and ceramic for various applications.<sup>1</sup> However, to improve the quality of the deposited films for desired application, a sound understanding of the plume dynamics, and physical and chemical properties of the ablated species is required, since laser-ablated plume is the source of thin films in PLD. Laser-ablated plume primarily consists of electrons, ions, neutrals, and ionized species. As the plume expands in an ambient medium the ablated species from the target undergo collisions with the atoms, molecules of the ambient resulting in scattering and slowing down of the plume. The peripheral region of the expanding plume constitutes predominantly particles of high kinetic energy; the collisional processes get enhanced by high reactivity of the charged species<sup>2</sup> that may help in the formation of oxides or nitrides<sup>3</sup> or small clusters.<sup>4</sup> The hydrodynamic expansion of the plume, the composition, and size distribution of clusters depend not only on initial conditions, but also on the laser intensity, pulse width, and ambient gas pressure. The growth and deposition of the films are determined by the thermodynamic parameters of the target material and initial conditions such as temperature and density of the vapor ejected after ablation. Hence, the understanding of plasma formation and

its expansion dynamics is imperative for optimization of PLD and processing of high-quality thin film. The plume generated by laser ablation is dynamic in nature both spatially and temporally. To understand the dynamics of the plume, several diagnostics, such as optical emission spectroscopy (OES),<sup>5</sup> plume imaging (fast photography),<sup>6</sup> ion probes,<sup>7</sup> interferometry (pump-probe),<sup>8</sup> and time-of-flight mass spectroscopy (TOFMS),<sup>9</sup> have routinely been used.

With recent attention towards short-wavelength lasers for use in high-density storage devices<sup>10</sup> and to have material for UV and blue light-emitting devices<sup>11,12</sup> considerable efforts are underway to understand the ablation characteristics of II-VI material. Zinc oxide (ZnO) has been of much interest to researchers due to its wide band gap of 3.3 eV (direct) at room temperature, high exciton binding energy of 60 meV, significantly larger than that of ZnSe (22 meV) and GaN (25 meV), its higher radiation hardness (compared to Si), and its alloy ability with MgO. Due to high melting point ZnO can withstand high annealing temperature and treatment processing associated with doping and contact formation. It implies that a ZnO-based device would not degrade fast due to low defect generation and would last comparatively (compared to GaN) longer. There are several reports of lasing action at room temperature due to excitonic transitions.<sup>13,14</sup> ZnO polycrystalline thin film and powder act as disordered dielectric media where lasing originates from random scattering in the medium.<sup>15</sup> There are recent reports of random lasing even with low density of ZnO nanorods<sup>16</sup> where strong transverse confinement of light inside ZnO is achieved by depositing MgO buffer layer over ZnO nanorods. The versatility of ZnO is further enhanced due to its ability to make alloy at different concentration and different temperature with MgO.<sup>17,18</sup> Since PLD is a nonequilibrium

<sup>a)</sup>Author to whom correspondence should be addressed; electronic mail: thareja@iitk.ac.in

process, it has extensively been employed to deposit thin films that are reported to far exceed the thermodynamic limit of solubility of MgO. Ohtomo *et al.*<sup>19</sup> demonstrated the synthesis of high-quality, single-phase, hexagonal  $Mg_xZn_{(1-x)}O$  thin films with Mg concentrations up to 33 at. %. In the cubic phase, the phase diagram predicts solubility of ZnO in cubic MgO lattice up to 40 at. %, however, recently this limit is reportedly being stretched through wide range.<sup>17</sup> ZnO is a piezoelectric material and has applications in surface acoustic wave (SAW) devices such as resonators and filters. Although, polymeric materials show high third-order optical nonlinearity<sup>20</sup> in subpicosecond time scale and find applications in all-optical switching devices,<sup>21</sup> they are prone to degradation due to thermal and aging effects. However, inorganic materials, such as ZnO, with high melting point and response to nonlinear optical effects make it a suitable choice.

Several techniques are being used to produce ZnO thin films, such as molecular-beam epitaxy (MBE), metal-organic chemical-vapor deposition (MOCVD), magnetron sputtering, and PLD.<sup>15,22,23</sup> PLD has also been used to deposit nanoclusters of various sizes.<sup>4,5</sup> The nanoscale one-dimensional (1D) materials have been proposed or demonstrated to have superior mechanical toughness, higher luminescence efficiency, enhancement of thermoelectric figure of merit, and a lowered lasing threshold.<sup>24</sup> In this paper we have used PLD to produce ZnO thin film. OES is used as a tool to optimize the conditions for deposition of thin films of ZnO in ambient atmosphere of oxygen. The deposited films were characterized by atomic force microscopy (AFM). The deposited films are shown to exhibit third-harmonic generation (THG) that depended on the particle size of ZnO in thin films. We also report the variation in band-gap energy by varying the concentration of MgO in the film. This property can be exploited to produce high-performance thin-film detectors and light sources tailored to the end-user requirement in the UV region.

## II. EXPERIMENTAL DETAILS

The experimental setup used here is similar to the one described elsewhere.<sup>11</sup> The plasma of ZnO was formed by focusing third harmonic [355 nm, pulse width of 5-ns full width at half maximum (FWHM)] of *Q*-switched neodymium: yttrium aluminum garnet (Nd:YAG) pulsed laser with repetition rate of 10 Hz to a focused spot size of 250  $\mu$ m. The OES studies of ZnO target were carried out both in vacuum and ambient oxygen at varying pressures. In order to have fresh target surface and to avoid drilling as the laser beam impinges on the surface, the disk-shaped ZnO (99.99% pure) target pellet was rotated continuously by a microprocessor-controlled stepper motor. The sample was kept inside a vacuum chamber at a base pressure of less than  $10^{-4}$  Torr. In order to record the various constituents of plasma emission lines, plasma was imaged on to the one end of the fiber coupled to a monochromator (Jobin-Yvon HRS-320). An intensified charge-coupled device (ICCD) camera (DH 720, Andor Technology) was used at the exit slit of the monochromator to record spectrum at different distances

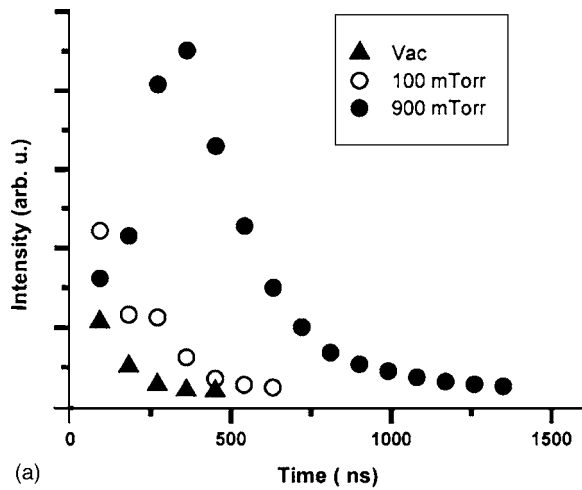
from the target at various delays with respect to the ablating pulse at constant laser intensity of  $2.04 \times 10^{10}$  W/cm<sup>2</sup> both in oxygen ambient and vacuum. The optical time-of-flight (OTOF) measurements were done varying the position of the plasma by imaging on to the monochromator (Jobin Yvon, HRS-2), recorded using a photomultiplier (Hamamatsu, rise time of 2.2 ns) at the exit slit of the monochromator, and fed on to a fast Digital Oscilloscope (500 MHz, Agilent Technologies, USA). The films were deposited under similar conditions as that of plasma study in a different chamber fitted with turbomolecular pump (TMP) (Pfeiffer-63MM) backed by rotary pump. The pellets of different molar concentration of MgO-doped ZnO,  $Mg_xZn_{(1-x)}O$  alloys were prepared by homogeneously mixing MgO and ZnO in appropriate proportions and sintered at 1000 °C for 5 h. The chamber was evacuated to a base pressure of  $4 \times 10^{-6}$  Torr prior to introduction of oxygen. The deposition time was 45 min at substrate temperatures ranging from 200 to 500 °C in steps of 100 °C. The ablated material was deposited on the glass substrate placed at 4 cm away from the target surface. The films of thickness of 120 nm as measured using stylus method profilometry were obtained. The crystal structure of deposited films was studied with x-ray-diffraction (XRD) measurement using  $Cu K\alpha$ , 1.54 Å. The laser energy used was the same as that used in plasma study.

## III. RESULTS AND DISCUSSION

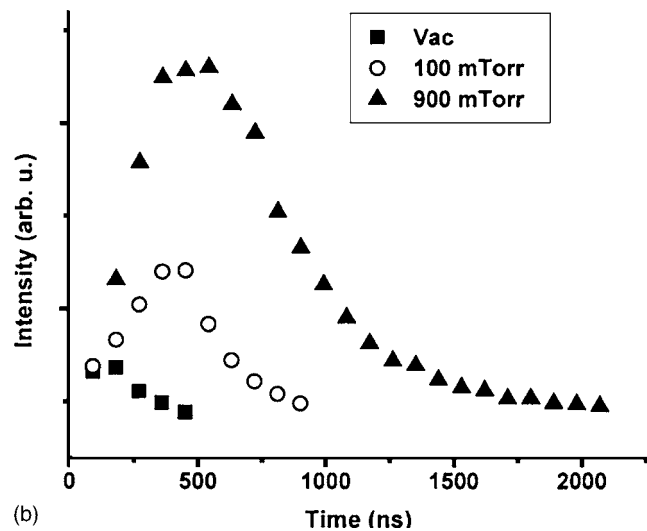
### A. Dynamical evolution of ZnO plasma

The plasma species in the plume make collisions among themselves and the background gas thermalizing their energy resulting in the condensation and eventual deposition as clusters onto a suitably placed substrate. The temporally and spatially resolved plasma emission spectra of ZnO were recorded normal and parallel to the target surface in vacuum and in ambient oxygen. At a distance close to the target surface (<2 mm) an intense continuum emission was observed. With the increase in delay time with respect to ablating pulse the intensity of continuum decreases gradually and the discrete transitions corresponding to neutral and low ionic states were observed. Various transitions in the emission spectra were identified using the standard table and the data available in the literature.<sup>25</sup> The observed line intensities are higher in ambient gas as compared to vacuum. As the plasma expands in ambient gas highly energetic particles produced in the early stage of plasma undergo collisions with the ambient atmosphere resulting in enhanced cooling. The process in turn helps to deposit films with appropriate stoichiometric conditions.

The dynamic nature of the laser-created plasmas makes the atomic and ionic populations evolve both in time and space within the plasma plume. The temporal and spatial behaviors of fast expanding plume are studied by recording the emission spectrum of the Zn I transition  $s^4d\ 3D - s^4p\ 3P$  at 328.23-nm,  $s^4d\ 3D - s^4p\ 3P$  at 330.26-nm,  $s^4d\ 3D - s^4p\ 3P$  at 334.5-nm,  $s^5s\ 3S - s^4p\ 3P$  at 468.01-nm,  $s^5s\ 3S - s^4p\ 3P$  at 472.21-nm,  $s^5s\ 3S - s^4p\ 3P$  at 481.05-nm lines, Zn II transition at 491.16 and 492.6 nm, and O I transition ( $3s\ ^5S^0 - 3p\ ^5P$ ) at 777 nm, respectively. We observed



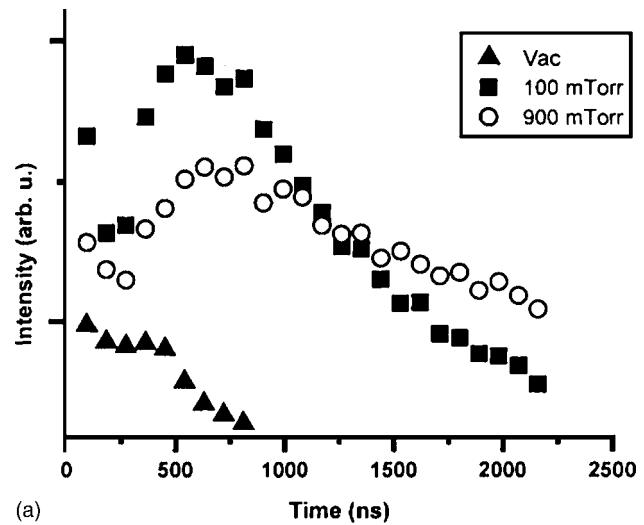
(a)



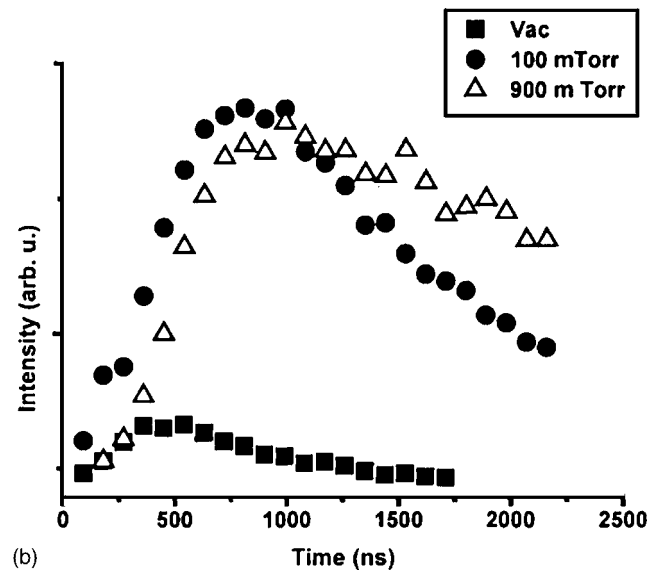
(b)

FIG. 1. Temporal variation of intensity of Zn II (491 nm) species at spatial distance of (a) 4 mm and (b) 6 mm in vacuum, 100 and 900 mTorr of oxygen.

a striking difference in the evolution of Zn I and Zn II transitions in vacuum and ambient gas environments. The line intensity of Zn II increases with an increase in ambient gas pressure, while neutral Zn I attains maximum intensity at 100 mTorr of ambient oxygen and then decreases with further increase in pressure. Various neutrals as well as ionic species survive for longer time in the presence of ambient gas. The confinement of the plasma to a smaller volume results in higher intensity of emission lines. Figures 1(a) and 1(b) show the intensity variation of the most intense line of Zn II at 492.6 nm at various temporal delays in vacuum, 100- and 900-mTorr ambient oxygen. The singly ionized zinc lines are more intense at an ambient of 900 mTorr than at 100 mTorr of oxygen. Figures 2(a) and 2(b) show the intensity variation of the most intense line of Zn I at 481 nm at various temporal delays under ambient gas conditions. The intensity ratio of Zn II species at 900 to that at 100 mTorr of oxygen ambient at spatial distances of 4 and 6 mm is 2.1 and 2.4, respectively. The abundance of higher ionized species implies a large concentration of particles with higher energy reaching/hitting the substrate and hence affecting the quality



(a)



(b)

FIG. 2. Temporal variation of intensity of Zn I (481 nm) lines at spatial distance of (a) 4 mm and (b) 6 mm in vacuum, 100 and 900 mTorr of oxygen.

of the deposited films. However, the intensity ratio of Zn I species at 900 to that at 100 mTorr of oxygen ambient at spatial distances of 4 and 6 mm is 0.74 and 0.9. We also observe from the OES data, the intensity for the O I at 777 nm to be more at 100 mTorr of oxygen ambient as compared to vacuum and 900 mTorr.

The temporal evolution of the recorded OES spectra at 2 mm for Zn II species shows that it survives for 210 ns for vacuum, 330 and 720 ns for 100 and 900 mTorr of oxygen, respectively. Thus, for better quality of the deposited films higher pressure (900 mTorr) is not desirable, for ionized species with high kinetic energy are likely to induce large structural and stress disorder during film growth.<sup>26</sup>

Figure 3 shows a bar diagram of the variation of integrated intensity of OES with respect to distance from the target for Zn II (491.16 and 492.6 nm) in various ambient conditions. The intensity of Zn II gradually increases as we move away from the target surface for 900 mTorr ambient pressure, Fig. 3(a). Figure 3(b) shows the spatial variation of intensity of Zn I transition in various ambient conditions. The

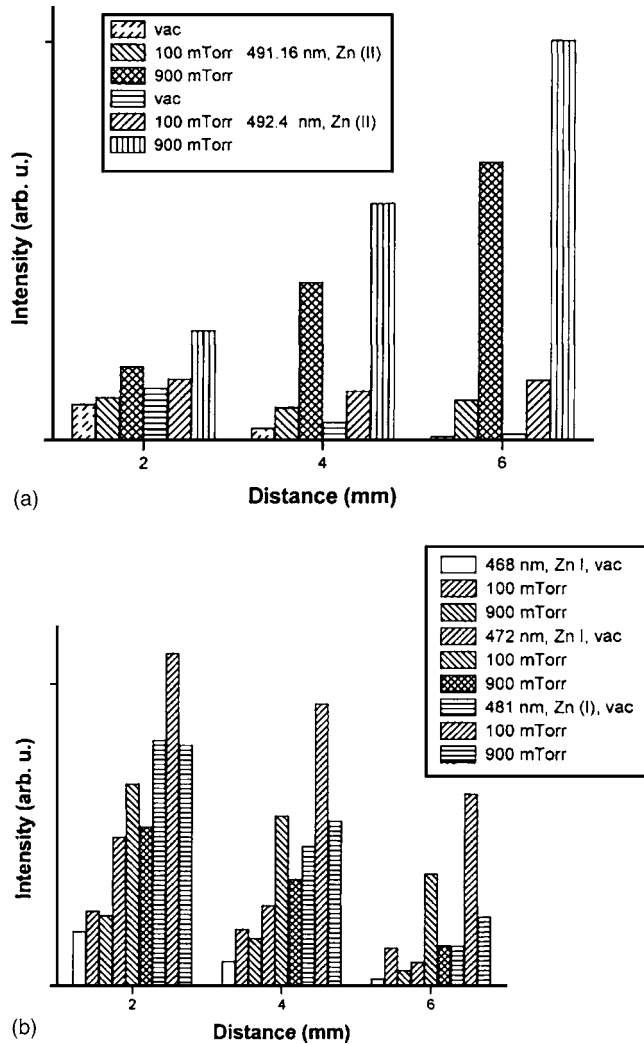


FIG. 3. The integrated intensity of Zn I and Zn II species in (a) 100 and (b) 900 mTorr of oxygen.

ratio of intensity of Zn I at 481 nm at 100 mTorr to that at 900 mTorr is found to be 1.38, 1.71, and 2.77 at 2, 4, and 6 mm away from the target, respectively. This implies most efficient formation of Zn I at 100 mTorr at all distances compared to at 900 mTorr.

Assuming the system in local thermodynamical equilibrium<sup>27</sup> (LTE) we estimated electron temperature of 3.6 eV at 2 mm away and parallel to the target surface in ambient of 100 mTorr of oxygen using O II emission lines. The Boltzmann plot of transitions  $3s^2D-3p^2P^0$  at 391.19 nm,  $3s^2P-3p^2P^0$  at 395.43 nm,  $3s^2P-3p^2P^0$  at 397.32 nm,  $3p^4D^0-3d^4F$  at 407.21 nm,  $3p^4D^0-3d^4F$  at 407.58 nm,  $3p^4P^0-3d^4D$  at 411.92 nm,  $3p^4P^0-3d^4P$  at 415.33 nm,  $3p^2F^0-3d^2G$  at 418.54 nm, and  $3p^2F^0-3d^2G$  at 418.98 nm was used for calculating temperature. The electron density of  $1 \times 10^{19} \text{ cm}^{-3}$  is obtained using the stark-broadened profile of O II transition  $3s^4P-3p^4S^0$  at 371.2 nm.

The time evolution of various transitions at 391.19 nm (O II), 468.01 and 472.21 nm (Zn I), and 491.16 nm (Zn II) at various spatial distances (2–8 mm) from the target surface using photomultiplier tube (PMT) coupled at the exit slit of monochromator was investigated. The velocity of each of the

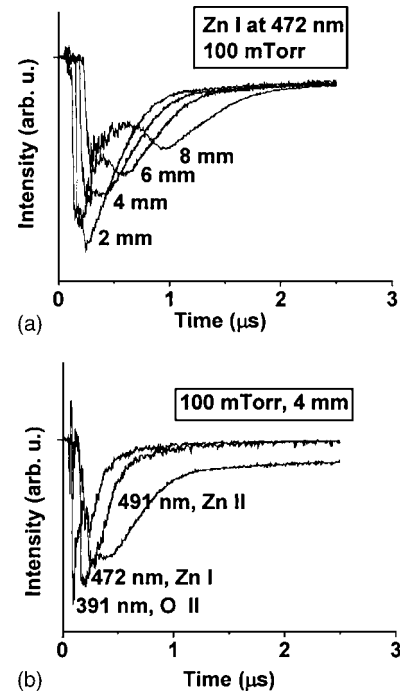


FIG. 4. (a) OTOF spectra of Zn I (472 nm) line at various distances in 100 mTorr of oxygen, and (b) OTOF spectra of Zn I (472 nm), Zn II (491 nm), and O II (391 nm) line at 4 mm in 100 mTorr of oxygen.

species is calculated from the delay of the peak of the signal at different distances with respect to the trigger pulse.<sup>28</sup> In order to estimate the expansion velocities for various emitting species within the plume many transient OTOF spectra were recorded at different distances from the target. The velocities of O II from OTOF were  $3.3 \times 10^6$ ,  $1.7 \times 10^6$ , and  $0.3 \times 10^6$  cm/s in vacuum, 100 and 900 mTorr of ambient oxygen, respectively. We observed that the velocity of ionic and neutral species is different and can be explained in terms of mobility which is proportional to charge-to-mass ratio ( $q/m$ ). As the plasma expands in vacuum, the electrons strive to overtake the ions resulting in an uncompensated space charge and electric field that decelerates the electrons and accelerates ions resulting in higher velocity for high ionic states.

Figure 4(a) shows the OTOF behavior of Zn I line at various spatial distances in ambient atmosphere of 100 mTorr. In vacuum, the plume expands freely and the species collide only with the plasma species and hence relatively there is no significant change in the velocity. However, in the ambient atmosphere the collisions with the ambient gas atoms, molecules the velocity of Zn I and Zn II decrease considerably because of the drag force experienced by the plasma plume front. Figure 4(b) shows the OTOF profile of various species at a fixed distance of 4 mm and ambient pressure of 100-mTorr oxygen. We observe a peculiar interesting feature of double peak structure in the pressure dependence of the OTOF spectrum. Figure 5 shows the OTOF spectrum for Zn I at 4 mm both in vacuum and in ambient oxygen. The appearance of slow components at later time is clearly seen at 100 mTorr. The slow component may be due to recombination of Zn II into Zn I at later times due to collision process, implying that an efficient recombination at

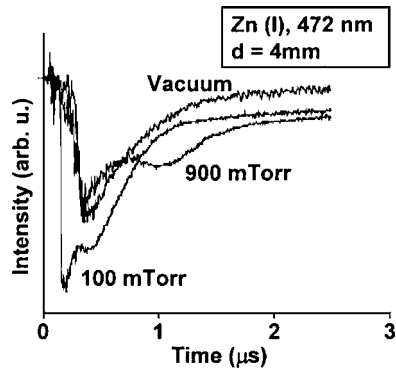


FIG. 5. The OTOF spectra of Zn I at 4 mm in vacuum and in oxygen.

100 mTorr compared to that at 900 mTorr for the emergence of second peak is less prominent. The double peaked behavior has been reported in earlier studies of laser-produced plasma either by OES or by imaging techniques in graphite, aluminum, etc.<sup>28</sup> Thus, the increase in Zn I at 100 mTorr might help to get a stoichiometric film of ratio Zn:O at 1:1 as reported in the pulsed laser deposition.<sup>15,29</sup> Since the Coulomb collision cross section depends on the velocity and charge, various species in the plume will have different cross section,  $\sigma_c \propto (q/v)^4$ , where  $q$  is the charge of zinc species and  $v$  is the velocity of the species. As the velocity of Zn II is less in 900 mTorr compared with 100 mTorr, the cross section for Zn II is higher at 900 mTorr compared to that at 100 mTorr. The observed intensity of the emitted lines of Zn II by OES at 900 mTorr being maximum might be warding off other species in the plume and hence destroy the appropriate composition of Zn and O. In the same token, the Zn I has a maximum intensity at 100 mTorr as compared to Zn II. Figures 6(a) and 6(b) show the temporal variation in the intensity of Zn I, Zn II, and O I at 100 and 900 mTorr, respectively. Presuming that the emitted intensity is proportional to the number density of the corresponding species, the presence of respective species at appropriate spatial region and temporal interval might dictate the stoichiometry of the deposited film, as shown Fig. 3.

### B. Plume dynamics of the laser-ablated ZnO

To investigate the plume dynamics of ZnO plasma in vacuum and an ambient oxygen pressure we recorded plume images using ICCD camera (DH 720, Andor Technology) at different delay times with respect to the ablating pulse.<sup>30</sup> Figure 7 shows the recorded images of ZnO plasma at a fluence of  $2 \times 10^{10}$  W/cm<sup>2</sup> in ambient gas pressure of 100 mTorr of oxygen. It follows from the figure that the presence of an ambient gas slows down the plume in ambient of oxygen relative to the propagation in vacuum. As the plume expands in ambient gas, a compressed region is formed between the plasma and the ambient gas. This compressed region propagates ahead of the plume with a velocity more than the local sound velocity in the medium  $c_s = (\langle Z \rangle kT/m)^{1/2}$  and generates shock wave.  $\langle Z \rangle$  is the average ion charge,  $k$  is the Boltzman constant,  $T$  is the electron temperature, and  $m$  is the ion mass. According to the shock wave model the shock position is given by the relation

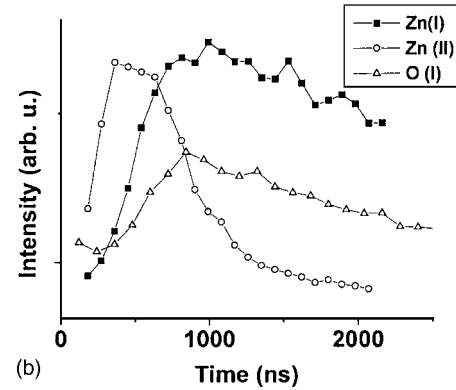
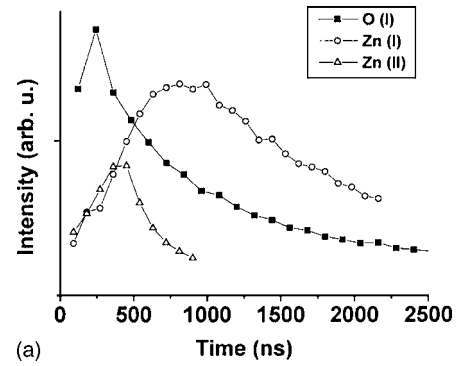


FIG. 6. Temporal variation of intensity of Zn I (481 nm), Zn II (492 nm), and O I (777 nm) in (a) 100 and (b) 900 mTorr of oxygen at fixed distance of 6 mm from the target.

$R(t) = \xi_0 (E_0/\rho_0)^{1/5} t^{2/5}$ , where  $\xi_0$  is a constant,  $E_0$  is the amount of energy released, and  $\rho_0$  is the ambient gas density.<sup>31</sup> The  $R-t$  (plume front position with respect to the delay time) plot at 100 mTorr shows a dependence  $R(t) \propto t^{0.36}$ . Shock wave formation has been reported at 100 mTorr in aluminum and yttrium-barium copper oxide (YBCO) in ambient nitrogen and oxygen.<sup>6,30</sup> The estimated plume velocity from the images in the ambient of 100 mTorr at a delay of 100 ns was  $3.5 \times 10^6$  cm/s while the estimated velocity of O II from OTOF was  $1.7 \times 10^6$  cm/s, consistent with the measurement taken by complementary setup.

The recorded plasma plume images are the direct manifestation of ejected species from the target. Since the plume images at different delay times are snapshots of spatial variation of all the species, the evolution of the species at a fixed distance is a series of snapshots of a specified species. The

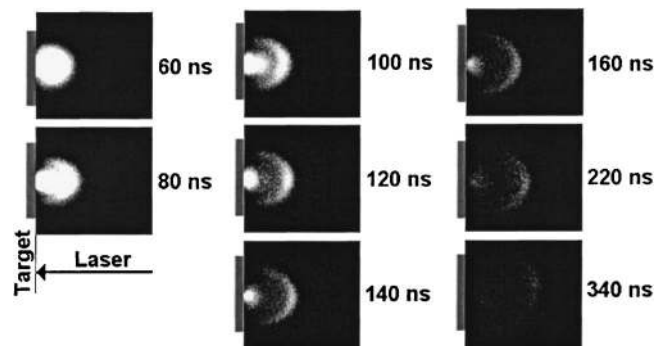


FIG. 7. ICCD images of expanding ZnO plume in 100 mTorr of oxygen.

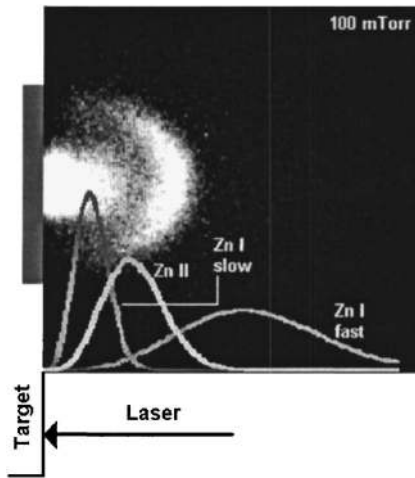


FIG. 8. ICCD image of ZnO plume in 100 mTorr of oxygen showing shifted-Maxwellian distribution with Zn I (472 nm) and Zn II (491 nm) emission lines.

temporal evolution of a species at a fixed point can be transformed into velocity distribution. Since the recorded intensity from the emitted species follows statistic result, one can assume that the intensity distribution within the plasma follows shifted-Maxwellian distribution,<sup>32</sup>

$$f(v) \propto v^3 \exp\left[-\frac{m(v - v_{cm})^2}{2kT}\right]. \quad (1)$$

Figure 8 shows the fitted shifted-Maxwellian distribution of Zn I and Zn II in 100-mTorr oxygen exhibiting the emergence of dual peak that corresponds to fast and slow moving components of Zn I.

### C. Thin-film deposition

#### 1. Deposition of ZnO and $Mg_xZn_{(1-x)}O$ films

In order to be consistent with spectroscopic observations we deposited ZnO and  $Mg_xZn_{(1-x)}O$  films at various substrate temperatures at 100 and 900 mTorr of ambient oxygen pressures. We see the emergence of a cubic phase at 50 molar % of MgO. Since Si is a cubic system, this could bring about a huge difference in the processing of these optically active materials as this opens a horizon of possibilities of integrating them with existing Si-based technology. The ablated material is deposited on the glass substrate kept at 4 cm from the target surface. The films of thickness of 120 nm as measured using stylus method profilometry were obtained. The crystal structure of the deposited films was studied with XRD measurement using  $Cu K\alpha$ , 1.54 Å. The XRD of the films deposited at 100 mTorr was highly oriented along (002) plane. However, the films deposited at higher pressures showed (101), (002), and (100) planes, similar to our earlier observation.<sup>15</sup> The result is in agreement with our analysis of spectroscopic investigations of plume where we observed that predominance of Zn I species at 100 mTorr may help in getting quality films. Taking 100 mTorr as optimum ambient pressure in our experiment we deposited  $Mg_xZn_{(1-x)}O$  alloy thin films with  $x$  from 0.1 to

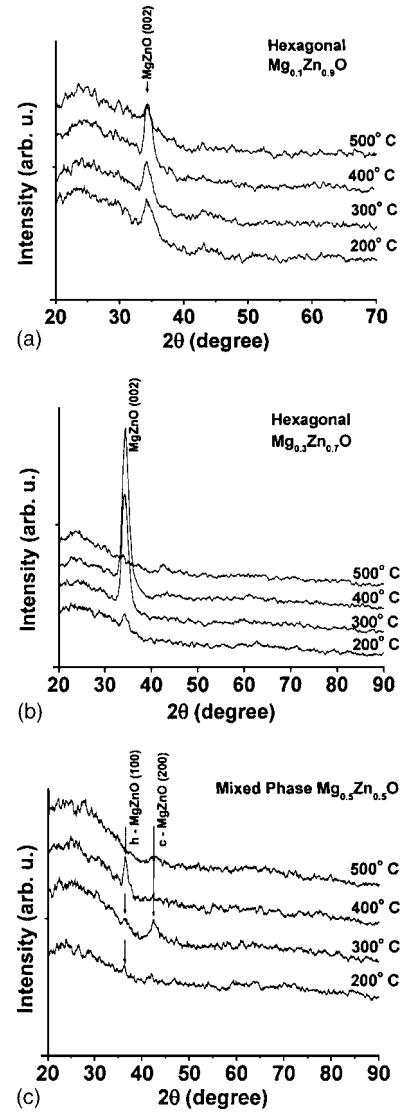


FIG. 9. X-ray-diffraction patterns of  $Mg_xZn_{(1-x)}O$  thin films deposited by ablating  $Mg_xZn_{(1-x)}O$  target containing (a) 0.1, (b) 0.3, and (c) 0.5 molar % of MgO at different substrate temperature in 100 mTorr of oxygen.

0.5.  $Mg_{0.1}Zn_{0.9}O$ ,  $Mg_{0.3}Zn_{0.7}O$ , and  $Mg_{0.5}Zn_{0.5}O$  were grown on glass substrates at 200, 300, 400, and 500 °C at 100-mTorr  $O_2$ .

The x-ray-diffraction patterns of  $Mg_xZn_{(1-x)}O$  alloy films with Mg molar % of 0.1, 0.3, and 0.5 are shown in Fig. 9. Figures 9(a) and 9(b) shows the dominance of (002) plane, being of minimum surface energy and hence energetically a highly preferred orientation. This suggests the  $c$ -axis, columnar growth, perpendicular to the substrate. We did not observe any other orientation in our samples. The films are essentially single crystalline. A hump in the initial part ( $2\theta = 20^\circ - 30^\circ$ ) is due to amorphous substrate. The intensity of (002) peak is more at 400 °C compared to other temperatures for all samples. For  $x=0.1$ , Fig. 9(a), the (002) peak appears to be temperature dependent and does not occur at its standard value of 34.45 ( $2\theta$ ). At substrate temperatures of 200, 300, and 500 °C peak appears at 34.2° and the corresponding calculated lattice constant is 5.24 Å, however, the peak shifts towards lower value for 400 °C at 34.1° with  $c = 5.25$  Å. For  $x=0.3$  [Fig. 9(b)], the peak appears at 34.2°

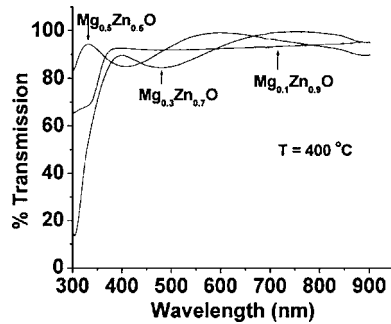


FIG. 10. Optical transmission spectra of thin films with 0.1, 0.2, and 0.3 molar % of MgO deposited at 400 °C showing blueshift with increase in MgO content.

with  $c=5.24$  Å. It shifts towards higher angle of  $34.4^\circ$  at 400 °C with value of  $c=5.21$  Å. The temperature behavior is attributed to different thermal-expansion coefficients of ablated material and substrate. However, no peak is observed at 500 °C implying an amorphous nature of deposited film at this temperature. The XRD of samples with  $x=0.5$  is entirely different. There is no signature of peak at  $34.4^\circ$  for (002) orientation in the patterns. Instead we obtained mixed phase that constitutes both hexagonal and cubic phases. The hexagonal peak corresponding to (100) appears which is unusual for ZnO-based thin films. However, there appears another peak at  $42.4^\circ$ , corresponding to (200) of cubic  $Mg_xZn_{(1-x)}O$  that becomes prominent at 300 °C. The lattice spacing slightly shifts from the standard value of 4.2 to 4.24 Å. To sum up we observe single peak implying crystalline growth or presence of hexagonal phase along with the formation of nanoparticles for  $x=0.1$  and 0.3 whereas a mixed phase is observed  $x=0.5$ . It is worth mentioning that both hexagonal and cubic phase coexist for  $x=0.5$  and have same lattice spacing calculated using both the peaks for the mixed phase.

The optical transmittance spectra for band-gap determination were recorded using double beam spectrophotometer (Jasco-V550) in the UV-vis-NIR (300–900 nm). Since the glass substrate has strong absorption below 300 nm we could not record the absorption edge for  $Mg_{0.5}Zn_{0.5}O$  samples. All our samples were highly transparent (>85%) throughout the visible region, as shown in Fig. 10. This particular property is well suited for transparent conductive films and solar blind detectors. The band-gap measurements could be done only with  $x=0.1$  and 0.3 samples since with  $x=0.5$  concentration the absorption edge shifted below 300 nm where glass shows very high absorption. Figure 11 shows the variation in band gap for thin-film samples with MgO molar % of 0.1 and 0.3 at different substrate temperatures. The band gap of films was determined using Tauc plot where  $[\alpha h\nu]^2$  was plotted against photon energy  $h\nu$ . A typical Tauc plot is shown as an inset in Fig. 11. The band gap increases with Mg concentration and deposition temperature. The increase in band gap with temperature is attributed to higher vapor pressure of Zn and ZnO compared to MgO. The higher vapor pressure of Zn and ZnO leads to more diffusion of ZnO from the film at higher temperature so that the contribution from MgO is further increased. The theoretical values of band gap obtained using virtual crystal approximation (VCA),<sup>17</sup>

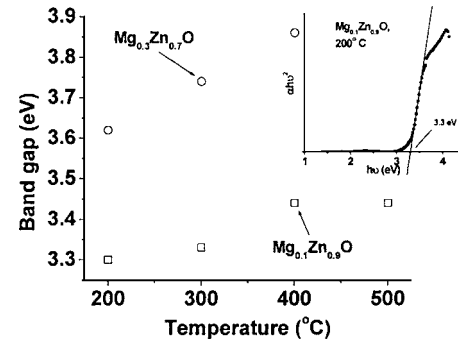


FIG. 11. Band-gap variation of  $Mg_{0.1}Zn_{0.9}O$  and  $Mg_{0.3}Zn_{0.7}O$  films with substrate temperature. A typical plot of Tauc plot is shown in the inset.

$$E_g(Mg_xZn_{(1-x)}O) = E_g(MgO)^*x + E_g(ZnO)^*(1-x),$$

are 3.78 and 4.65 eV for  $x=0.1$  and 0.3, respectively. The band gap for Mg (0.3) at 500 °C could not be calculated due to the presence of Urbach band-tail states. The second peak in Fig. 12 is attributed to the amorphous nature of the film. Evidently, the x-ray diffraction of this film also confirmed its amorphous nature.

Surface morphology of the films was studied using AFM (Molecular Imaging, USA, Model: Pico Scan-4) in a noncontact mode. The surface morphology of the films deposited at 400 °C for different concentration is shown in Fig. 13. The surface morphology of the fabricated films depends, apart from other factors, on deposition temperature and ambient pressures. The root-mean-square (rms) roughness ( $1 \times 1$ - $\mu m^2$  scanned area) decreases from 16 to 8 nm with the increase of Mg content from  $x=0.1$  to 0.3 and remains comparable for  $x=0.5$  at 7 nm, close to the reported values.<sup>33</sup> Similarly, the temperature variation also reveals the minimum rms roughness for 400 °C films, however, further increase in temperature increased the rms roughness very rapidly. This is in agreement with the XRD data where best crystalline behavior is observed at 400 °C. Figures 13(a) and 13(b) show a typical  $3 \times 3$ - $\mu m^2$  scan area for  $Mg_{0.3}Zn_{0.7}O$  sample at 300 and 400 °C, the particle size can be clearly differentiated. Figure 13(c) shows three-dimensional (3D) AFM images indicating that the film growth is highly oriented along the  $c$  axis, normal to the substrate surface.

To sum up, we have deposited thin films of  $Mg_xZn_{(1-x)}O$  alloy at different substrate temperatures using pulsed laser deposition technique. The films deposited at 400 °C were

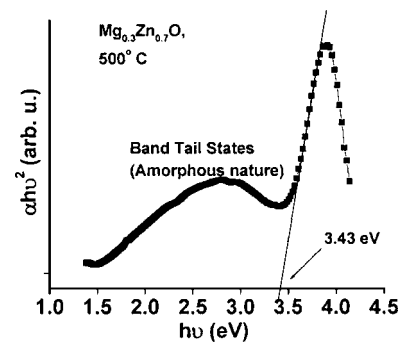


FIG. 12. A typical Tauc plot for amorphous film showing Urbach band-tail states for  $Mg_{0.3}Zn_{0.7}O$  film deposited at 500 °C.

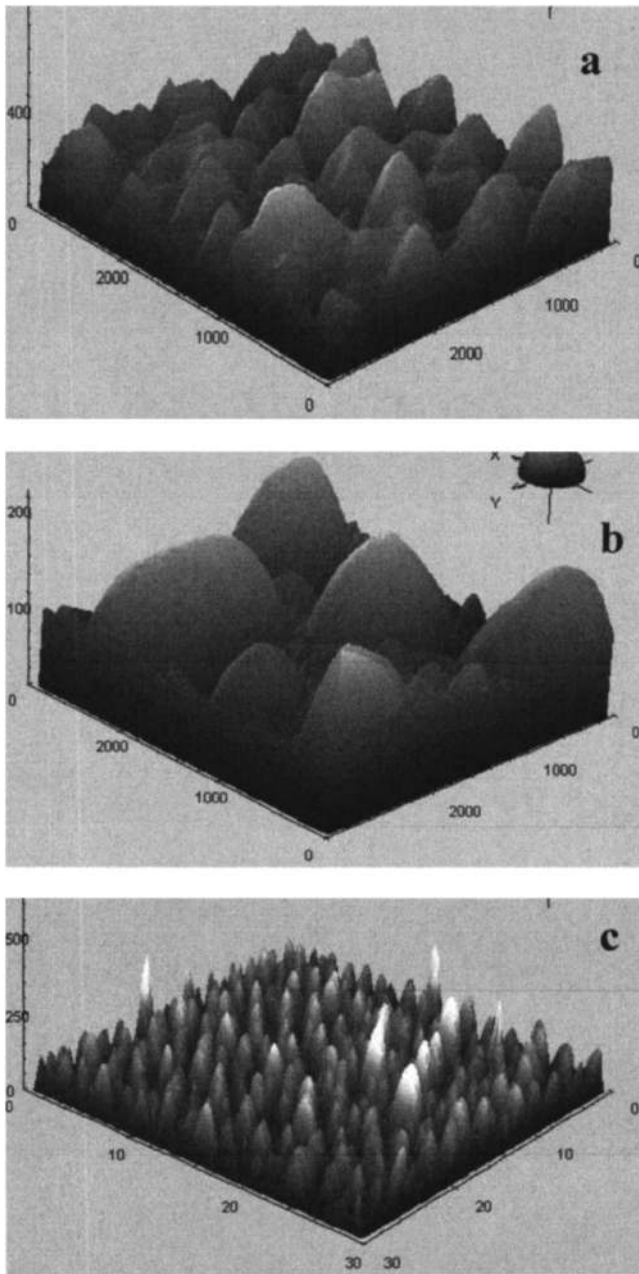


FIG. 13. AFM images of  $Mg_{0.3}Zn_{0.7}O$  films exhibiting increase of particle size for (b) 400 °C compared to (a) 300 °C for the scan area of  $3 \times 3 \mu m^2$ . A larger scan area of  $30 \times 30 \mu m^2$  (c) shows that film is highly  $c$  axis oriented which is also evident from x-ray diffraction.

found to be best both in terms of crystalline and roughness. Interestingly, all the films were found to be amorphous at 500 °C, whereas various researchers have reported films to be crystalline up to 800 °C. The glass substrate could have played a vital role. A blueshift in the absorption edge with the increase in Mg content is observed. The band gap is observed to increase with deposition temperature due to higher vapor pressure of ZnO compared to MgO.

## 2. Nonlinear properties of ZnO films

THG is a nonlinear process in which incident, high intensity laser radiation at a frequency  $\omega$ , interacting with a nonlinear medium, results in the generation of an additional

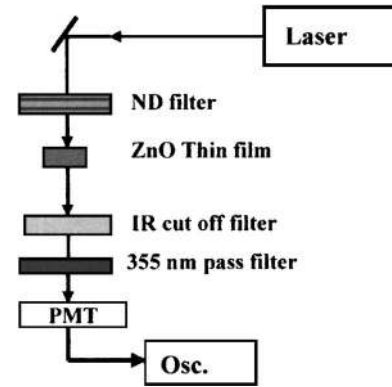


FIG. 14. Experimental setup for harmonic generation. PMT is photomultiplier tube and ND is a neutral density filter.

spectral component at the frequency  $3\omega$  and given by the equation as a function of  $\omega$  and  $2\omega$ ;  $3\omega = \omega + 2\omega$ . In order to characterize THG it is necessary that we look at second harmonic generation (SHG) in the film. The size and roughness of the films used for investigating nonlinear properties were estimated by scanning the films over the areas ranging from  $500 \times 500$  to  $2 \times 2 \mu m^2$ . The AFM images showed size and roughness, respectively, of 8 and 15 nm, 84 and 150 nm for the films deposited at 100 and 900 mTorr, respectively.

Figure 14 shows the typical setup used for the measurement of second and third harmonic generated in the films. A Q-switched Nd:YAG laser (1064 nm, 8 ns, and 10 Hz) was used as a fundamental beam for the study of second-harmonic generation in transmission mode. The input energy of the fundamental is attenuated using the Schott filter. The energy of the fundamental beam was measured using energy/power meter (Ophir model: Nova, 10A-P, QTL) in the path of the beam. A quartz lens was used to focus the fundamental beam into the film. An IR cutoff filter was kept after the film to block the residual IR coming from the films. In order to vary the incident angle of the fundamental beam on the film the sample placed on a rotating platform was continuously varied. A narrow band interference pass filter (Newport, USA) centered at 532 nm ( $\pm 2$  nm) was kept after IR blocking filter which allows only the second harmonic generated by the fundamental. However, for measurement of third harmonic the interference pass filter (Coherent, USA) used was centered at 355 nm ( $\pm 3$  nm). The generated second harmonic (third harmonic) was monitored using a PMT, it is ensured that no other light enters PMT so as to have a signal free from interference of any other light source. The output of the PMT was connected to an oscilloscope triggered by the laser output. The intensity of the second harmonic generated by the fundamental beam is given by<sup>34</sup>

$$I_{2\omega} = \frac{128\pi^3 (t_{af}^{-1}\gamma)^4 (t_{fs}^{-2p})^2 (t_{sa}^{-2p})^2}{cA (n_{2\omega} \cos \theta_{2\omega})^2} \times I_{\omega}^2 \left( \frac{2\pi L}{\lambda} \right)^2 [\chi_{\text{eff}}^{(2)}]^2 \frac{\sin^2 \varphi}{\varphi^2}, \quad (2)$$

where  $A$  is area of the beam spot,  $I_{\omega}$  is the intensity of the incident fundamental beam,  $L$  is the films thickness,  $n_{\omega}$  ( $n_{2\omega}$ ) is the refractive index at the fundamental (second harmonic)

frequency in the ZnO film, and  $\theta_\omega$  ( $\theta_{2\omega}$ ) is determined by  $\sin \theta = n_\omega \sin \theta_\omega$  ( $\sin \theta = n_{2\omega} \sin \theta_{2\omega}$ ). Phase angle  $\varphi$  is given by

$$\varphi = \frac{2\pi L}{\lambda} (n_\omega \cos \theta_\omega - n_{2\omega} \cos \theta_{2\omega}), \quad (3)$$

where  $t_{af}^{1\gamma}$  represents the Fresnel transmission coefficient of the fundamental beam from air to film, and  $\gamma$  indicates the polarization direction.  $t_{fs}^{ap}$  and  $t_{sa}^{2p}$  represent the Fresnel transmission coefficient of the second-harmonic beam from the ZnO film to the substrate and from the substrate to air. Now, if the incident angle  $\theta$  changes continuously then  $\theta_\omega$  and  $\theta_{2\omega}$  also change resulting in the change of coherence length. Variation of second-harmonic intensity versus incident angle produces a fringe pattern called Maker fringes.  $\chi_{\text{eff}}^{(2)}$  in Eq. (1) represents the effective second-order susceptibility of the ZnO thin film. To get  $\chi_{\text{eff}}^{(2)}$  for the films from the experimental observations using Eq. (1) we need to know  $I_\omega^2/A$ . Using known second-harmonic coefficient of KDP crystal, the value of  $I_\omega^2/A$  was estimated for the given experimental conditions. The films deposited at 100 mTorr of ambient oxygen showed large second-harmonic coefficient as compared to 900 mTorr of oxygen. The values of  $\chi_{\text{eff}}^{(2)}$  of ZnO thin films were 3.2 and 0.7 pm/V for 100 and 900 mTorr, respectively.

The intensity of third harmonic  $I_{3\omega}$  in terms of the incident intensity of the fundamental beam  $I_3$  in a thin film is given by<sup>35</sup>

$$I_{3\omega} = \frac{64\pi^2}{c^2} (A)\chi^{(3)}(I_\omega)^3 f_a, \quad (4)$$

where

$$f_a = \frac{[1 - \exp(-\alpha_{3\omega}d/2)]^2 + (\Delta\varphi)^2 \exp(-\alpha_{3\omega}d/2)}{(n_{3\omega}^2 - n_\omega + k_{3\omega})^2 + (2n_{3\omega}k_{3\omega})}.$$

Here  $\chi^{(3)}$  is the nonlinear susceptibility and  $d$  is the thickness of the film,  $n_\omega$  and  $n_{3\omega}$  are the refractive indices at fundamental and third harmonic,  $\alpha_{3\omega}$  and  $k_{3\omega}$  are the linear absorption coefficient and the imaginary refractive index at third harmonic,  $\Delta\varphi$  is the phase mismatch in the nonlinear medium between fundamental- and third-harmonic frequencies,  $c$  is the velocity of the light, and  $A$  is an empirical factor that depends on the geometry of the experimental setup. The magnitude of the third-order nonlinear susceptibility [ $\chi^{(3)}$ ] is given by<sup>35</sup>

$$\chi^{(3)} = [\chi_s^{(3)}](2l/\pi)(l_{c,s}/l)(I_{3\omega}/I_{3\omega,s})^{1/2}, \quad (5)$$

where  $\chi_s^{(3)}$  is third-order nonlinear susceptibility of the substrate,  $l_{c,s}$  is the coherence length of substrate,  $l$  is the coherence length of the thin-film material,  $I_{3\omega}$  is the measured intensity of  $3\omega$  for the thin film, and  $I_{3\omega,s}$  is the measured intensity of  $3\omega$  for the substrate. We measured value of  $\chi^{(3)} = 9.56 \times 10^{-12}$  esu for the film deposited at 100 mTorr of oxygen ambient which is large compared to ZnO bulk crystal [ $\chi^{(3)} = 1.2 \times 10^{-13}$  esu]. THG signal as a function of fundamental frequency showed a cubic dependence on pump intensity, as shown in Fig. 15.

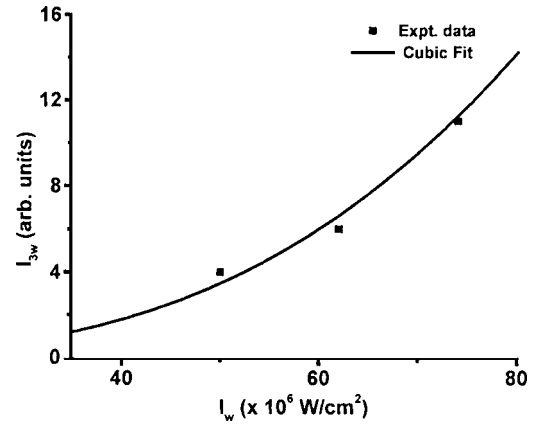


FIG. 15. Variation of THG signal measured as a function of fundamental intensity.

## IV. CONCLUSIONS

We have reported the spatial and temporal evolutions of the ZnO plasma using OES, OTOF, and ICCD imaging techniques. The intensity for Zn I species increases with pressure but is found to be more for 100 mTorr than that for 900 mTorr for distances  $>2$  mm. The time-resolved OES of ZnO under vacuum and oxygen ambient showed that the line intensity for neutral Zn species is large in 100-mTorr oxygen compared to that in vacuum and 900 mTorr of oxygen, therefore it can be used to optimize the deposition pressure for deposition of nanocrystalline ZnO thin films for better surface morphology. The investigations are used to arrive at an optimum ambient pressure for depositing  $\text{Mg}_x\text{Zn}_{(1-x)}\text{O}$  alloy thin films of different molar % of MgO, i.e.,  $x$  (0.1, 0.3, and 0.5). The absorption edge is blueshifted with an increase of  $x$  and deposition temperature. The deposited films exhibited high degree of transparency ( $>85\%$ ) over visible range. The deposited films exhibited nonlinear properties as manifested by SHG and THG in the films.

## ACKNOWLEDGMENT

Work is partly supported by DST (New Delhi) and DRDO (New Delhi).

- <sup>1</sup>Laser Ablation and Desorption, edited by J. C. Miller and R. F. Haglan, Jr. (Academic, New York, 1998).
- <sup>2</sup>P. E. Dyer, A. Issa, and P. H. Key, Appl. Phys. Lett. **57**, 186 (1990).
- <sup>3</sup>A. K. Sharma and R. K. Thareja, J. Appl. Phys. **88**, 7334 (2000).
- <sup>4</sup>D. B. Geohegan, A. A. Puretzky, G. Duscher, and S. J. Pennycook, Appl. Phys. Lett. **72**, 2987 (1998).
- <sup>5</sup>V. Narayanan and R. K. Thareja, Appl. Surf. Sci. **222**, 382 (2004).
- <sup>6</sup>D. B. Geohegan, Appl. Phys. Lett. **60**, 2732 (1992).
- <sup>7</sup>B. Toftmann, J. Schou, T. N. Hansen, and J. G. Lunney, Phys. Rev. Lett. **84**, 3998 (2000).
- <sup>8</sup>S. S. Mao, X. Mao, R. Greif, and R. E. Russo, Appl. Phys. Lett. **76**, 31 (2000).
- <sup>9</sup>V. Berardi, S. Amoroso, N. Spinelli, M. Armenante, R. Velotta, F. Fusco, M. Allegrini, and E. Arimondo, J. Appl. Phys. **76**, 8077 (1994).
- <sup>10</sup>S. D. Lester, F. A. Ponce, M. Geraford, and D. A. Steigerwald, Appl. Phys. Lett. **66**, 1249 (1995).
- <sup>11</sup>A. Mitra and R. K. Thareja, Mod. Phys. Lett. B **13**, 1075 (1999); R. K. Thareja and A. Mitra, Appl. Phys. B: Lasers Opt. **71**, 181 (2000).
- <sup>12</sup>H. Cao, Y. G. Zhao, S. T. Ho, E. W. Seelig, Q. H. Wang, and R. P. H. Chang, Phys. Rev. Lett. **82**, 181 (1999).
- <sup>13</sup>D. M. Bagnall, Y. F. Chen, Z. Zhu, T. Yao, S. Koyama, M. Y. Shen, and T. Goto, Appl. Phys. Lett. **70**, 2230 (1997).

- <sup>14</sup>Z. K. Tang, G. K. L. Wong, P. Yu, M. Kawasaki, A. Ohtomo, H. Koinuma, and Y. Segawa, *Appl. Phys. Lett.* **72**, 3270 (1998).
- <sup>15</sup>A. Mitra and R. K. Thareja, *J. Appl. Phys.* **89**, 2025 (2001).
- <sup>16</sup>S. F. Yu, C. Yuen, S. P. Lau, W. I. Park, and G.-C. Yi, *Appl. Phys. Lett.* **84**, 3241 (2004).
- <sup>17</sup>S. Chooapun, R. D. Vispute, W. Yang, R. P. Sharma, T. Venkatesan, and H. Shen, *Appl. Phys. Lett.* **80**, 1529 (2002).
- <sup>18</sup>S. Yang *et al.*, *Appl. Phys. Lett.* **82**, 3424 (2003).
- <sup>19</sup>A. Ohtomo *et al.*, *Appl. Phys. Lett.* **72**, 2466 (1998).
- <sup>20</sup>M. Hotzel, S. Urban, D. Egbe, T. Pautzsch, and E. Klemm, *J. Opt. Soc. Am. B* **19**, 2645 (2002).
- <sup>21</sup>Y. Guo, C. K. Kao, E. H. Li, and K. S. Chiang, *Nonlinear Photonics* (Springer, Berlin, 2002).
- <sup>22</sup>A. Mitra, R. K. Thareja, V. Ganesan, A. Gupta, P. K. Sahoo, and V. H. Kulkarni, *Appl. Surf. Sci.* **174**, 232 (2001).
- <sup>23</sup>R. D. Vispute *et al.*, *Appl. Phys. Lett.* **70**, 2735 (1997).
- <sup>24</sup>A. Ohtomo *et al.*, *Mater. Sci. Eng., B* **54**, 24 (1998).
- <sup>25</sup>W. L. Wiese and G. A. Martin, *Wavelengths and Transition Probabilities for Atoms and Atomic Transitions*, NSRDS—NBS 68 (U.S. Government Printing Office, Department of Commerce, Washington, DC, 1980).
- <sup>26</sup>D. P. Norton, C. Park, J. D. Budai, S. J. Pennycook, and C. Prouteau, *Appl. Phys. Lett.* **74**, 2134 (1999).
- <sup>27</sup>G. Bekefi, *Principles of Laser Plasmas* (Wiley Interscience, New York, 1976).
- <sup>28</sup>A. Neogi, A. Misra, and R. K. Thareja, *J. Appl. Phys.* **83**, 2831 (1998).
- <sup>29</sup>L. N. Dinh, M. A. Schildbach, M. Balooch, and W. McLean II, *J. Appl. Phys.* **86**, 1149 (1999).
- <sup>30</sup>A. K. Sharma and R. K. Thareja, *Appl. Phys. Lett.* **84**, 4490 (2004).
- <sup>31</sup>Y. Zel'dovich and Y. Raizer, *Physics of Shock Waves and High-Temperature Hydrodynamics* (Academic, New York, 1966).
- <sup>32</sup>P. R. Willmott, R. Tim, and J. R. Huber, *J. Appl. Phys.* **82**, 2082 (1997).
- <sup>33</sup>X.-L. Guo, H. Tabata, and T. Kawai, *J. Cryst. Growth* **223**, 135 (2001).
- <sup>34</sup>H. Cao, J. Y. Wu, H. C. Ong, J. Y. Dai, and R. P. H. Change, *Appl. Phys. Lett.* **73**, 572 (1998).
- <sup>35</sup>X. H. Wang, D. P. West, N. B. McKeown, and T. A. King, *J. Opt. Soc. Am. B* **7**, 1895 (1998).